Global and Planetary Change 88–89 (2012) 20–31

Contents lists available at SciVerse ScienceDirect

Global and Planetary Change

journal homepage: www.elsevier.com/locate/gloplacha

# Characteristics and mechanisms of sea surface height in the South China Sea

Jian Zhou, Peiliang Li *, Haili Yu

*Physical Oceanography Laboratory, Ocean University of China, Qingdao 266100, China*

ARTICLE INFO

*Article history:*
Received 23 November 2011
Accepted 1 March 2012
Available online 8 March 2012

*Keywords:*
Net heat flux
Freshwater
Wind stress
Stochastic dynamic analytic method
Markov model
Subsurface water

ABSTRACT

Fifty years (1960–2009) sea surface height (SSH) data derived from ECMWF ORA-S3 are analyzed in the South China Sea (SCS). Using stochastic dynamic analytic method to investigate characteristics of SSH on different timescales, it could be found that SSH in the SCS displays distinct seasonal (including annual and semi-annaul) and interannual variations. The annual signal has minimum value in February and maximum value in August, and its amplitude is 1.81 cm. The interannual SSH variability in the SCS is coherent with the ENSO/PDO/NPGO based on the lead-lag relationship. The seasonal SSH variations are induced by buoyancy fluxes and local wind stress. The local wind stress contribution to seasonal SSH in the east SCS is dominant (explain 20–65%), and buoyancy fluxes contribution is secondary (explain 30–40%). Buoyancy fluxes are determined by net heat fluxes in the upper ocean. Effect of freshwater fluxes can be neglected. Interannual variations are closely related to the subsurface water (depth about 100–300 m). ENSO/PDO/NPGO signals affect the temperature and salinity changes of the subsurface water and further lead to interannual variations of SSH.


## 1. Introduction

In terms of the physical mechanism research of SSH variations, a number of studies have been devoted to research the importance of various forcings and processes in explaining the SSH variations. Many studies address steric responses of sea level variations (Nerem et al., 1997; Stammer, 1997; Cazenave and Nerem, 2004; Carton et al., 2005; Lombard et al., 2005a, 2005b; Ishii et al., 2006;). Seasonal steric sea level change compared with TOPEX/Poseidon satellite altimeter data at different large spatial scales indicated that thermal effect accounts for much of the observed seasonal variability, especially when averaging over zonal regions. Some regional seasonal patterns of sea level anomalies in the tropical oceans are well represented by the thermal model prediction (Chen et al., 2000).

Other studies specifically focus on the mechanisms of dynamic response. A series of studies have discussed SSH adjusted via barotropic Rossby waves (Sturges and Hong, 1995; Frankignoul et al., 1997; Miller et al., 1998; Deser et al., 1999; Seager et al., 2001; Schneider et al., 2002; Qiu, 2002, 2003, Qiu and Chen, 2006; Taguchi et al., 2007; Sasaki et al., 2008; Zhang et al., 2011). The dominant processes affecting SSH variability observed by the TOPEX/Poseidon altimeter vary regionally in the Pacific: baroclinic Rossby waves, equatorially trapped Kelvin waves, steric response to surface heating and the response to wind stress curl forcing are all important (Vivier et al., 1999). In mid-latitudes, the most conspicuous feature in the large-scale changes in SSH is related to surface buoyancy fluxes, predominantly surface heat fluxes. The next prominent variability on subannual timescales is the adjustment of the ocean to varying winds stress fields in terms of planetary waves. SSH variations in the Pacific Ocean north of 40°N relative to the steric component can be described as a time-dependent Sverdrup balance is addressed for the Pacific Ocean (Stammer, 1997). The interannual SSH variability over the northeast Pacific Ocean is dominated by the local response to wind forcing based on reduced-gravity, quasi-geostrophic model includes linear damping (Cummins and Lagerloef, 2004). It demonstrated that a local Markov model driven by Ekman pumping can account for the variability and trend exhibited by the Station P time series as given by Cummins and Lagerloef (2002). Cabanes et al. (2006) demonstrated that the remaining SSH after correcting from local steric changes was relatively well explained by the quasi-steady barotropic Sverdup balance between 40° and 50°N. The large-scale adjustment to wind forcing via the propagation of Rossby waves agrees best with the remaining SSH in the 15–20°N region.

The SCS is the largest semi-enclosed marginal sea in the Asia. Under the influence of the monsoon, the Kuroshio, ENSO and some other factors, SCS becomes very active in dynamics. Affected by various factors, the SCS has significant multi-scale factures and patterns. By synthesizing previous studies, factors caused SSH are so complicated and varied. SSH mechanisms are variable spatially and on different timescales. In this paper, we study SSH in the SCS based on thermodynamics and dynamics. In terms of thermodynamics, steric sea level is mainly discussed, and the dynamics are analyzed based on the response to wind stress forcing. In addition, we also investigate the mechanism of interannual SSH variability. Efficiency of the mechanisms in predicting SSH is assessed by computing a local hindcast skill.

* Corresponding author. Fax: +86 532 66782850.
*E-mail address:* li.peiliang@gmail.com (P. Li).

0921-8181/$ – see front matter. 
doi:10.1016/j.gloplacha.2012.03.001

## 2. Data sources and data processing

### 2.1. Data sources

SSH, net heat fluxes and wind stress are provided by ECMWF ORA-S3. ORA-S3 is a new operational ocean analysis/reanalysis system which has been implemented at ECMWF. It has several innovative features, including an on-line bias-correction algorithm, the assimilation of salinity data on temperature surfaces and assimilation of altimeter-derived sea level anomalies and global sea level trends. The horizontal resolution is $1^\circ \times 1^\circ$, with the time period from 1960 through 2009 was used here. For further details of the model and assimilation see Balmaseda (2004), Anderson and Balmaseda (2005), Balmaseda et al. (2008), and Vidard et al. (2009).

The evaporation and precipitation from ERA-40 and ERA-Interim are used in this paper. The time range of them derived from ERA-40 is from January 1960 to December 1978. And ERA-Interim provides them for the period 1979–2009.

The monthly objectively analyzed subsurface temperature (version 6.9) for the period 1945–2010 is the most recently available dataset produced by Ishii et al. (2003, 2005) and Ishii and Kimoto (2009). The analysis is based on the latest version of World Ocean Database (WOD05) and World Ocean Atlas (WOA05) (Boyer et al., 2006) and a set of XBT observations compiled by the Japan Oceanographic Data Center. A near-real time data archive made available through the Global Temperature-Salinity Profile Program (GTSPP) is also used, which compensates the data sparseness of WOD05 since 1990. The spatial resolution of the data is $1^\circ \times 1^\circ$, with 24 standard depth levels to 1500 m. The vertical resolution decreases with depth by 0, 10, 20, 30, 50, 75, 100, 125, and 150 m, every 50 m to a depth of 300 m, and then every 100 m to a depth of 1500 m. The time period from 1960 through 2009 is used here.

### 2.2. Data processing

The freshwater fluxes are defined by the difference between evaporation and precipitation (denoted $EmnP = E - P$).

Following Kara et al. (2000), the mixed layer depth (MLD) is calculated in the SCS. The temperature and salinity data are from Ishii 6.9. In this study, the criterion on temperature shift applies 1.0 °C. The depth of 10 m from which the 'surface' values has been taken. This is included so we can avoid surface inversions or missing surface data. More details about the calculation method of MLD are given in Kara et al. (2000).

An equivalent-area weighting factor based on a simple cosine function of latitude should be applied to generate the mean sea level time series, diminishing the impact of data in high latitudes. The formula is listed below (Cazenave et al., 1998)

$$\overline{h_k} = \frac{\sum_i \sum_j h_{ijk} \cos\left(\phi_j\right)}{\sum_i \sum_j \cos\left(\phi_j\right)} \tag{1}$$

where $\overline{h_k}$ is the region-averaged SSH and k denotes the time; $i$ and $j$ denote the position at each grid point; $h_{ijk}$ is the SSH in grid of $(i, j)$ at time of $k$; $\phi_j$ is the latitude of the given grid. It is particularly worth noting that all time series are calculated based on Formula (1).

Efficiency of the mechanisms in calculating SSH is assessed by computing a estimation skill. Here, the estimation skill, $S$, is defined by

$$S = 1 - \frac{\left\langle \left(h_0 - h_p\right)^2 \right\rangle}{\left\langle {h_0}^2 \right\rangle} \tag{2}$$

where $h_0$ is the observed signal, $h_p$ is the modeled signal, and angle brackets denote a time averaging. Skill ranges between $-\infty$ and 1. High values for skill ($S \to 1$) indicate that observed and calculated SSH are both well correlated and of the same magnitude. Negative values denote low or negative correlations or larger magnitude for SSH.

## 3. Characteristics of SSH variations in the SCS

### 3.1. Variability of spatial-mean SSH

To extract the SSH on different timescales, we adopt stochastic dynamic analytic method in this study. The SSH time series $Y(t)$ can be written as:

$$Y(t) = T(t) + P(t) + X(t) + \alpha(t) \tag{3}$$

where $Y(t)$ is the average monthly SSH, $T(t)$ is the deterministic trend signals; $P(t)$ is the deterministic periodic signals; $X(t)$ is the residual random signals; $\alpha(t)$ is the white noise signals. Stochastic dynamic analytic method decomposes the variable into deterministic parts, periodic parts and random parts. As long as we give expressions and coefficients of deterministic and periodic parts, we can fit the original data and predict by extrapolation. For more information on stochastic dynamic analytic method, see Zuo et al. (1996).

Using stochastic dynamic analytic method to separate periodic signal of SSH, we can find SSH in the SCS displays seasonal and interannual variations. As shown in Fig. 1, SSH displays a distinct annual cycle with minimum in February and maximum in August. The seasonal amplitude of SSH is 2.8 cm, with the annual amplitude (1.81 cm), and semiannual amplitude (0.99 cm).

Fig. 1 also shows obviously that interannual variations signal, but the stronger seasonal and rising trend makes the interannual signal obscured. Thus appropriate filtering is needed for visualization of these signals. In this study, we remove the linear trend and signals with timescales shorter than 1 year to obtain the SSH residual (blue line in Fig. 1). To describe interannual variability better, comparisons between SSH residual and ENSO/PDO/NPGO index based on correlation analysis are shown in Fig. 2. As shown in Fig. 2a, the curve of SSH appears dominated by interannual fluctuations, particularly in the period 1972/1973, 1997/1998, 2009 (El Niño event) and 1975/1976, 1998–2000 (La Niña event). During El Nino (La Nina) year, SOI has a minimum (maximum) value and SSH is low (high). It is evidenced that the SSH variations in the SCS are strongly modulated by ENSO: their changes are the same phase, negative phase of SOI (El Niño event) corresponding to negative SSH; SOI positive phase (La Nina) corresponding to positive SSH. The synchronous correlation coefficient is 0.726. Fig. 2b is time series of PDO index and SSH. There is significantly negative correlation between SSH and PDO index (just opposite to SOI above, SOI is positive correlation). The correlation coefficient is −0.57. Fig. 2c also shows the North Pacific Gyre Oscillation (NPGO) have an opposite effect compared with PDO and it is fairly self-explanatory here. When PDO (NPGO) is warm (cold) phase, SSH have low values, vice versa.

It is also worthwhile to note that decadal signals, especially in 1960s, 1980s, 1990s, 2000s, SSH variations appear low values. After low-pass filtered over 10 years to the SSH residual (Fig. 3), the correlation coefficient of SSH and PDO is −0.2, and the correlation reaches up to −0.44 when SSH leads over PDO by 113 months. The correlation coefficient between SSH and NPGO is 0.7. The maximum correlation coefficient is 0.774 when NPGO leads SSH by about 11 months.

The interannual variability of SSH in the SCS is coherent with the ENSO/PDO/NPGO from the lead-lag relationship.

### 3.2. Spatial structure of SSH variability

SSH variability is not spatially uniform in the SCS, and we use the root-mean-square (RMS) method to obtain the spatial structure of

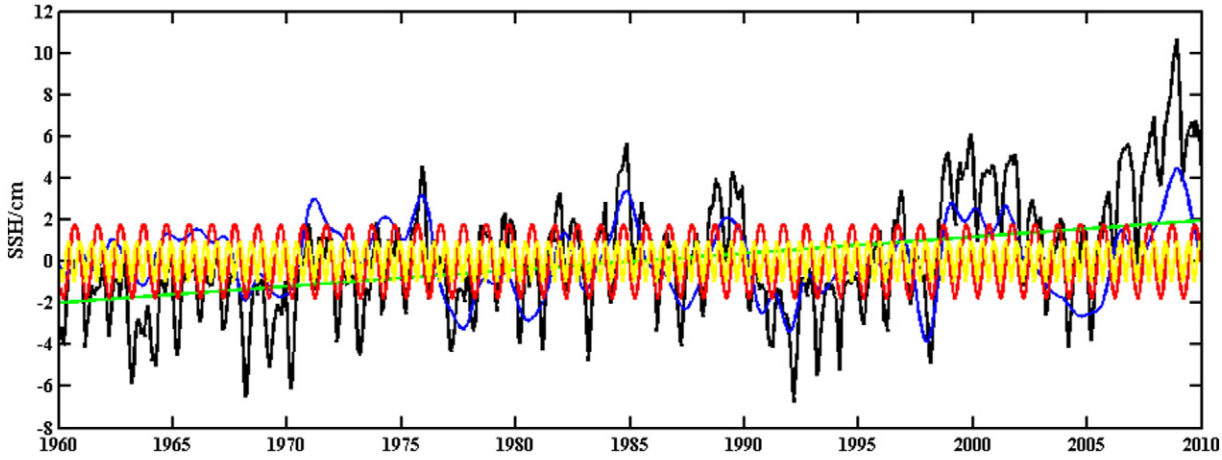


**Fig. 1.** Time series of the SSH averaged over the SCS: original SSH (black line), annual SSH (red line), semiannual SSH (yellow line) and the linear trend (green line, 7.9 mm/year). The blue line is low frequency signals based upon 13-month low-pass-filtered.

the SSH. A higher value of RMS of the area implies a dynamically active area. RMS values of the SSH are 7–9 cm in the east SCS (Fig. 4a). The largest variability, 9 cm RMS, occurs in the west Luzon Island where is the position of Luzon cold eddy. Fig. 4b shows RMS values of nonseasonal variability. High RMS (5–6 cm) in Fig. 4b are distributed over the Sulu Sea, which indicates that primarily interannual variations occur in this region. High RMS values distributed in Fig. 4a but low values in Fig. 4b near the Luzon Island indicate seasonal variations are primary in this region.

To better describe the temporal and spatial variability of the interannual SSH, we performed an empirical orthogonal function (EOF) analysis on the SSH data based upon 13-month low-pass-filtered. Fig. 5a shows the spatial pattern of the EOF; the associated amplitude time series is plotted in Fig. 5b. The amplitude time series of the first

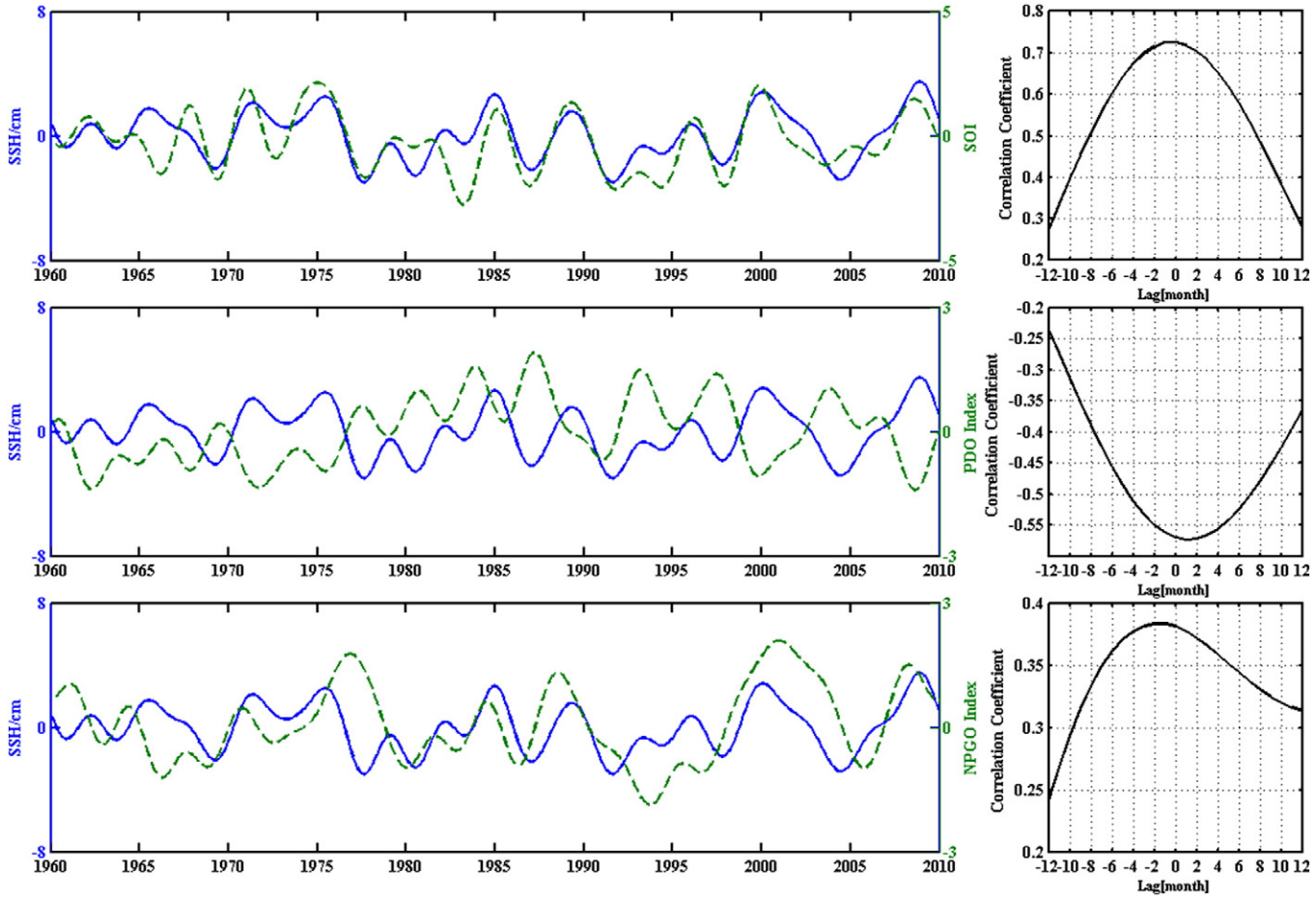


**Fig. 2.** Comparison between SSH (solid blue line) and climatic indices (SOI/PDO/NPGO) (dashed green line). Right plates are their lagged correlation. Positive lags here indicate the lead of SOI/PDO/NPGO over the SSH. Linear trend of SSH is removed. All variables are low-pass filtered (>32 months). SOI is from http://www.cgd.ucar.edu/cas/catalog/climind/SOI.signal.ascii; PDO Index is from http://jisao.washington.edu/pdo/PDO.latest; NPGO index is from http://www.o3d.org/npgo/data/NPGO.txt.

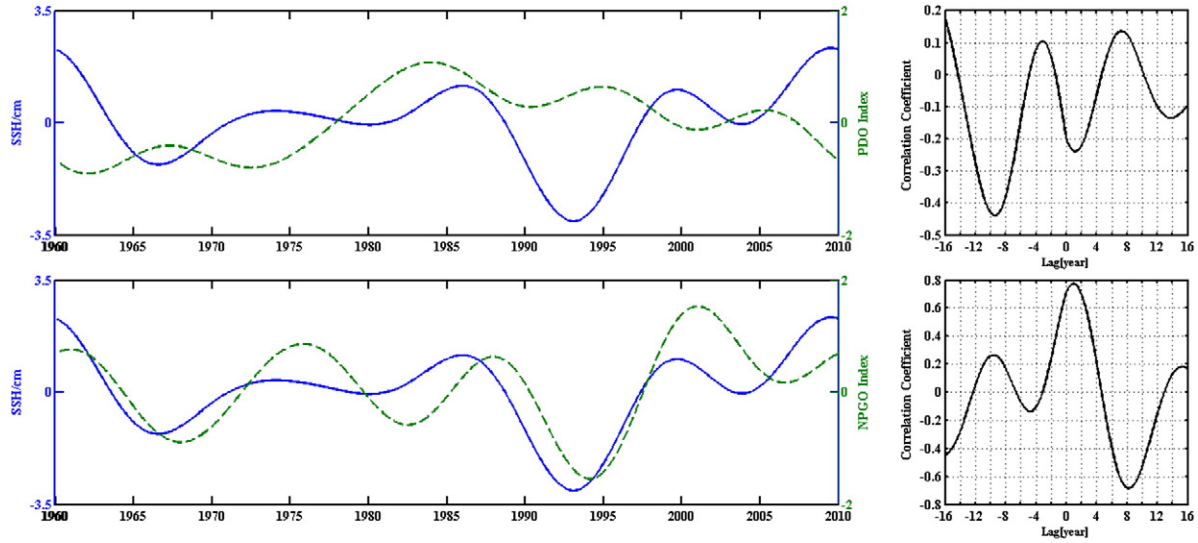


**Fig. 3.** Same as in Fig. 2, but low-pass filtered (>10 year).

mode shows primarily interannual variation. The first mode accounts for 84.38% of the total interannual variance. The spatial values of the first EOF are positive over the east SCS. High spatial values of the first EOF are distributed over the Sulu Sea. It also indicates interannual variations primarily occur in Sulu Sea. The amplitude time series of the first mode is normalized by its standard deviations and its relation with ENSO/PDO/NPGO are shown in Fig. 6. The results are consistent with that of stochastic dynamic analytic method in Fig. 2 and RMS method in Fig. 4.

In the following analyses, we investigate, in particular, mechanisms of seasonal and interannual SSH variations in the SCS.

## 4. SSH response to surface buoyancy forcing

Changes in temperature and salinity of a water column cause what are termed "steric" sea level variations (Patttullo et al., 1955). Steric sea level change due to thermal expansion as the thermosteric component (TC) and due to haline contraction as the halosteric component (SC) (Tabata et al., 1986). The total steric sea level (TSSL) change is the sum of TC and SC. TC, SC, and TSSL are calculated based on the following formulas:

$$\mathrm{TC} = \int_{z1}^{z2} \frac{1}{v}\frac{\partial v}{\partial T}\Delta T dZ \tag{4}$$

$$\mathrm{SC} = \int_{z1}^{z2} \frac{1}{v}\frac{\partial v}{\partial S}\Delta S dZ \tag{5}$$

$$\mathrm{TSSL} \gg \mathrm{TC} + \mathrm{C} \tag{6}$$

where $T$ is temperature, $S$ is salinity, $Z$ is depth, $z1$ and $z2$ are the lower and upper limits of depth of integration, $v$ is specific volume calculated as a function of temperature and salinity fields and pressure by the equation of state for sea water (EOS80) (UNESCO, 1987), and $\Delta T$ and $\Delta S$ are the monthly temperature and salinity deviation in reference to their climatological mean values at each layer, respectively. Total steric

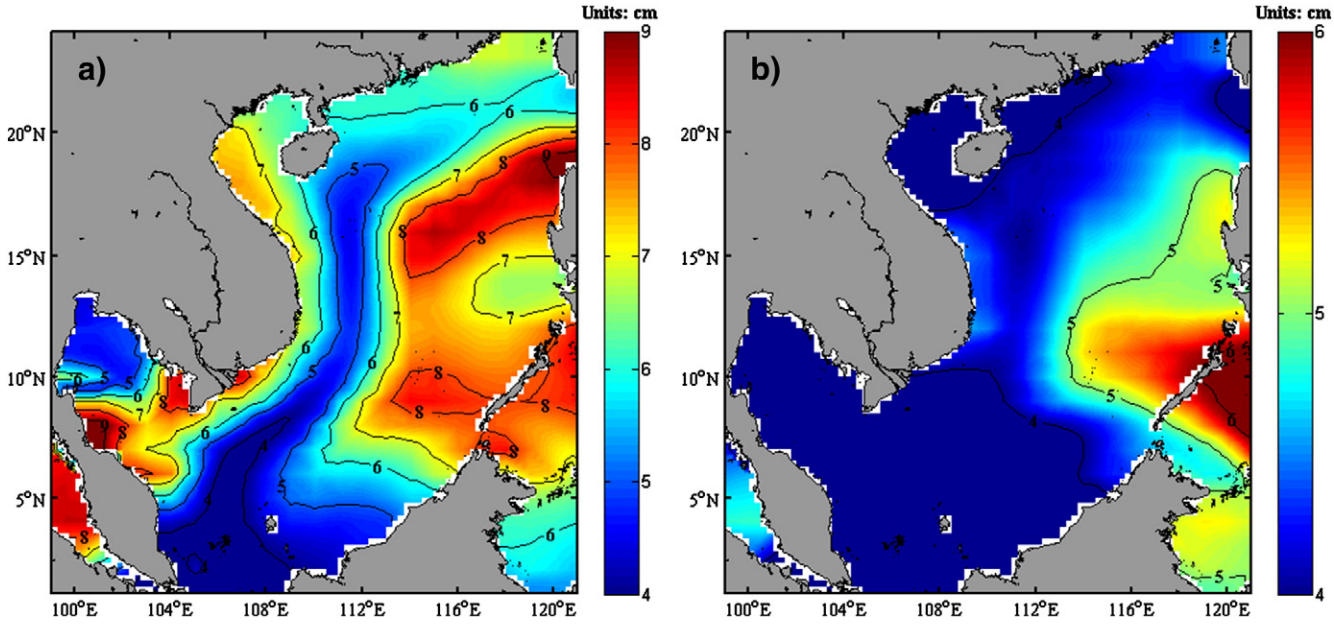


**Fig. 4.** a)Distribution of root-mean square (RMS) SSH and (b) RMS values of SSH based upon 13-month low-pass-filtered. The contour interval is 1 cm.

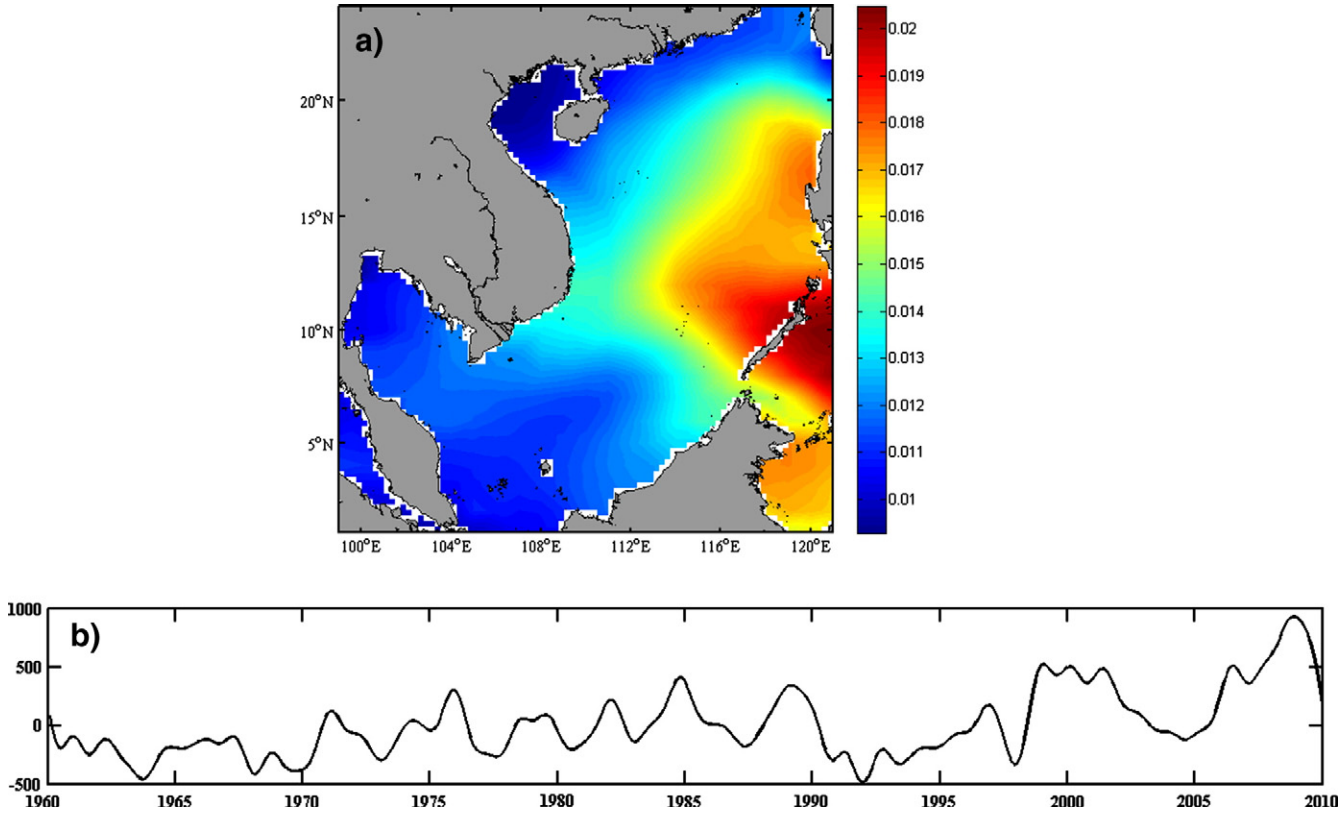


**Fig. 5.** First EOF mode of SSH based upon 13-month low-pass-filtered in the SCS. (a) Spatial pattern on top. (b) The amplitude time series of the first mode on bottom.

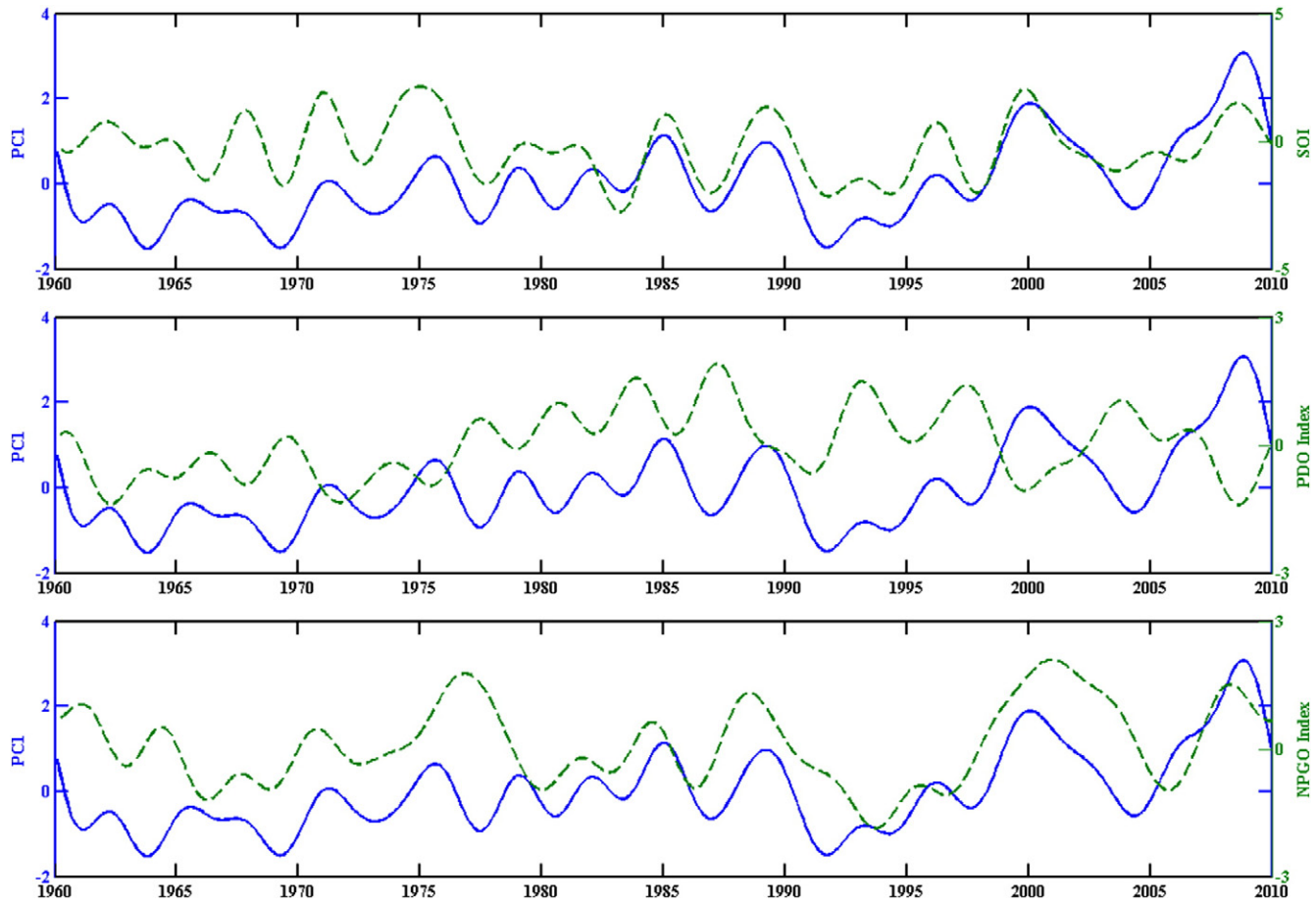


**Fig. 6.** The amplitude time serie of the first mode normalized by its standard deviations *vs.* SOI/PDO/NPGO. All variables are low-pass filtered (>32 months).

sea level anomaly at a layer is approximately the sum of temperature and salinity anomalies at that layer.

The integration is theoretically over the whole water column but, in practice, is limited to the upper part of the ocean, which is better sampled and is affected by atmospheric buoyancy fluxes. Changes in steric height can be caused either by buoyance flux including surface heating, fresh water flux (diabafic) or by vertical displacement of isotherms (adiabatic) by wind forcing (Vivier et al., 1999).

Following previous work (Stammer, 1997; Vivier et al., 1999), if we neglect diffusion and horizontal advection, the equation is given by

$$\frac{\partial h_s}{\partial t} = \frac{\alpha}{\rho_0 C_p}\left(Q(t) - \overline{Q(t)}\right) - \beta S_a(t)\left(\mathrm{EmnP}(t) - \overline{\mathrm{EmnP}(t)}\right) \quad (7)$$

where $h_s$ is the SSH dued to the buoyance flux, $\alpha$ is thermal expansion coefficient, $\beta$ is saline contraction coefficient, $\rho_0$ is the reference density, $C_P$ is specific heat of seawater constant pressure, $Q$ is the net heat flux, and EmnP is the fresh water flux. Diabatic steric height changes are dominated by the seasonal variations of density due to heating and cooling in the oceannic mixed layer (ML).

To evaluate $h_{\mathrm{heat}}$ and $h_{\mathrm{water}}$ from Eq. (7), we separately calculate them by following equations:

$$\frac{\partial h_{\mathrm{heat}}}{\partial t} = \frac{\alpha}{\rho_0 C_p}\left(Q(t) - \overline{Q(t)}\right) - \varepsilon_1 h_{\mathrm{heat}} \quad (8)$$

$$\frac{\partial h_{\mathrm{water}}}{\partial t} = -\beta S_a(t)\left(\mathrm{EmnP}(t) - \overline{\mathrm{EmnP}(t)}\right) - \varepsilon_2 h_{\mathrm{water}} \quad (9)$$

Eqs. (8) and (9) are derived from Eq. (7),but they increase dissipation term (the second term). Dissipative processes can significantly improve the calculated results.

In Eqs. (8) and (9), both $\alpha$ and $\beta$ are taken as the average value in the ML. The MLD is derived from Ishii 6.9. $Q(t)$ and EmnP($t$) are derived from ECMWF reanalysis (ERA-40 and ERA-Interim). In this study, $C_p = 4000\ \mathrm{J\cdot kg^{-1}\cdot K^{-1}}$. The calculated results are shown in Figs. 7 and 8.

Fig. 7a shows the plot of Correlation-Skill-$\varepsilon^{-1}$. $\varepsilon_1^{-1} = 150\ d$ is adopted as the dissipation coefficient in Fig. 7b–d. The seasonal amplitude of $h_{\mathrm{heat}}$ in the SCS is 2.3 cm including annual amplitude of 1.67 cm. $h_{\mathrm{heat}}$ displays significant seasonal variability (Fig. 7b). Fig. 7c and d shows distribution of correlations and skill between $h_{\mathrm{heat}}$ and SSH. There is a high correlation region in the northeast SCS, and their correlation coefficients exceed 0.5 (Fig. 7c). $h_{\mathrm{heat}}$ in this region can explain above 30% of SSH (Fig. 7d).

Fig. 8 shows the results of $h_{\mathrm{water}}$. The dissipation coefficient $\varepsilon_2^{-1}$ equals 200 $d$ (Fig. 8b–d). In the whole SCS, $h_{\mathrm{water}}$ has a small part in SSH. Although there are high correlations in the north SCS, $h_{\mathrm{water}}$ can only explain about 4%.

SSH induced by the buoyancy fluxes is determined by changes of heat fluxes in the upper ocean. The effect of fres$h_{\mathrm{water}}$ fluxes can be neglected.

## 5. Ekman pumping response

Wyrtki (1961) pointed out that seasonal characteristics of ocean circulation in SCS are mainly driven by the monsoon. Qu (2000) compared the wind field and hydrological observation data, and explicitly

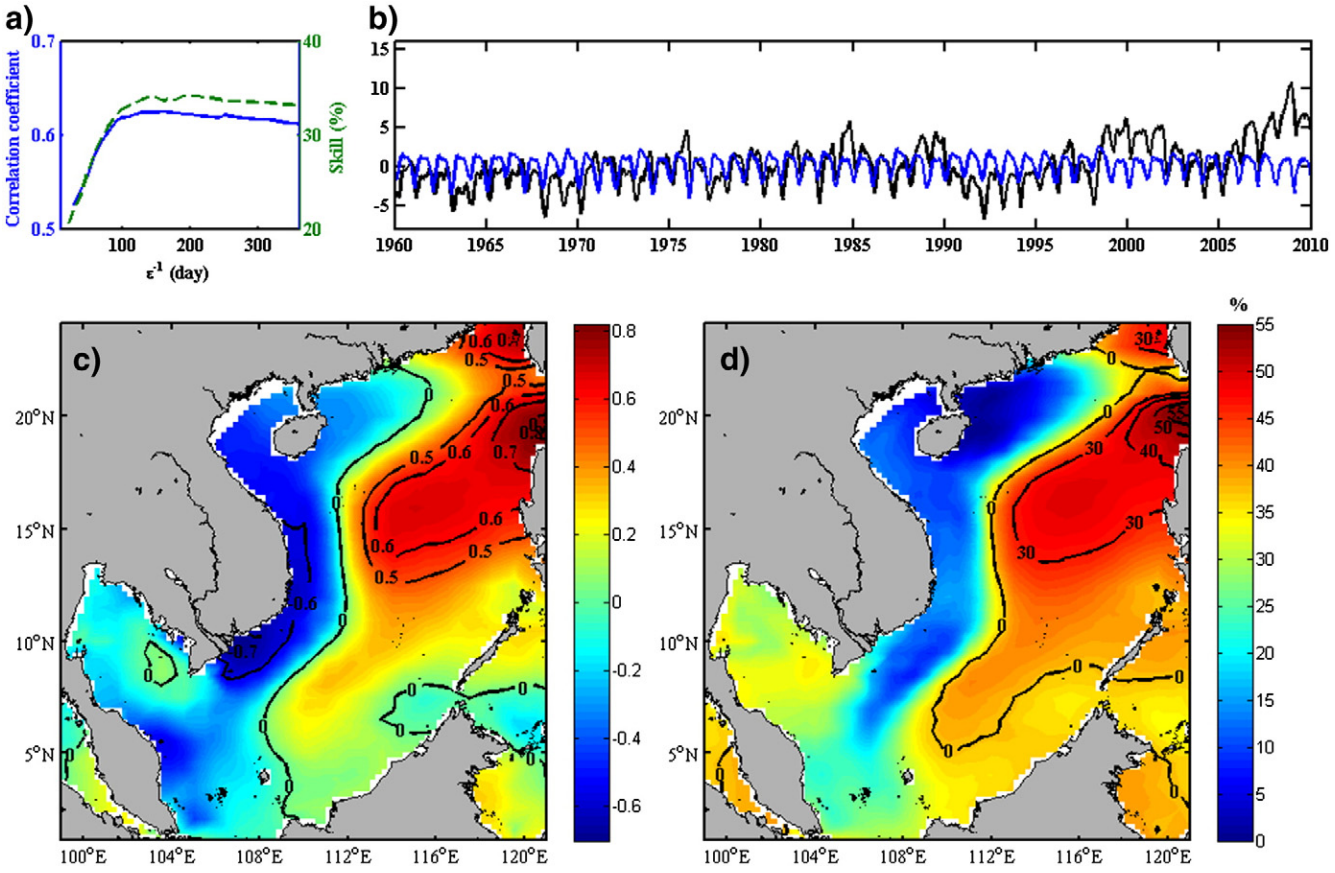


**Fig. 7.** (a) Correlation coefficient and skill of the $h_{\mathrm{heat}}$ as a function of the dissipation rate $\varepsilon$. (b) $h_{\mathrm{heat}}$ (blue line) vs. SSH (black line). (c) Correlations between $h_{\mathrm{heat}}$ and SSH. (d) Distribution of skill (%) of $h_{\mathrm{heat}}$ in accounting for the variance of SSH. Note, correlation coefficients exceeding 0.5 and skill exceeding 20% in the SCS are chosen in a). In (b)–(d), $\varepsilon_1^{-1} = 150\ d$.

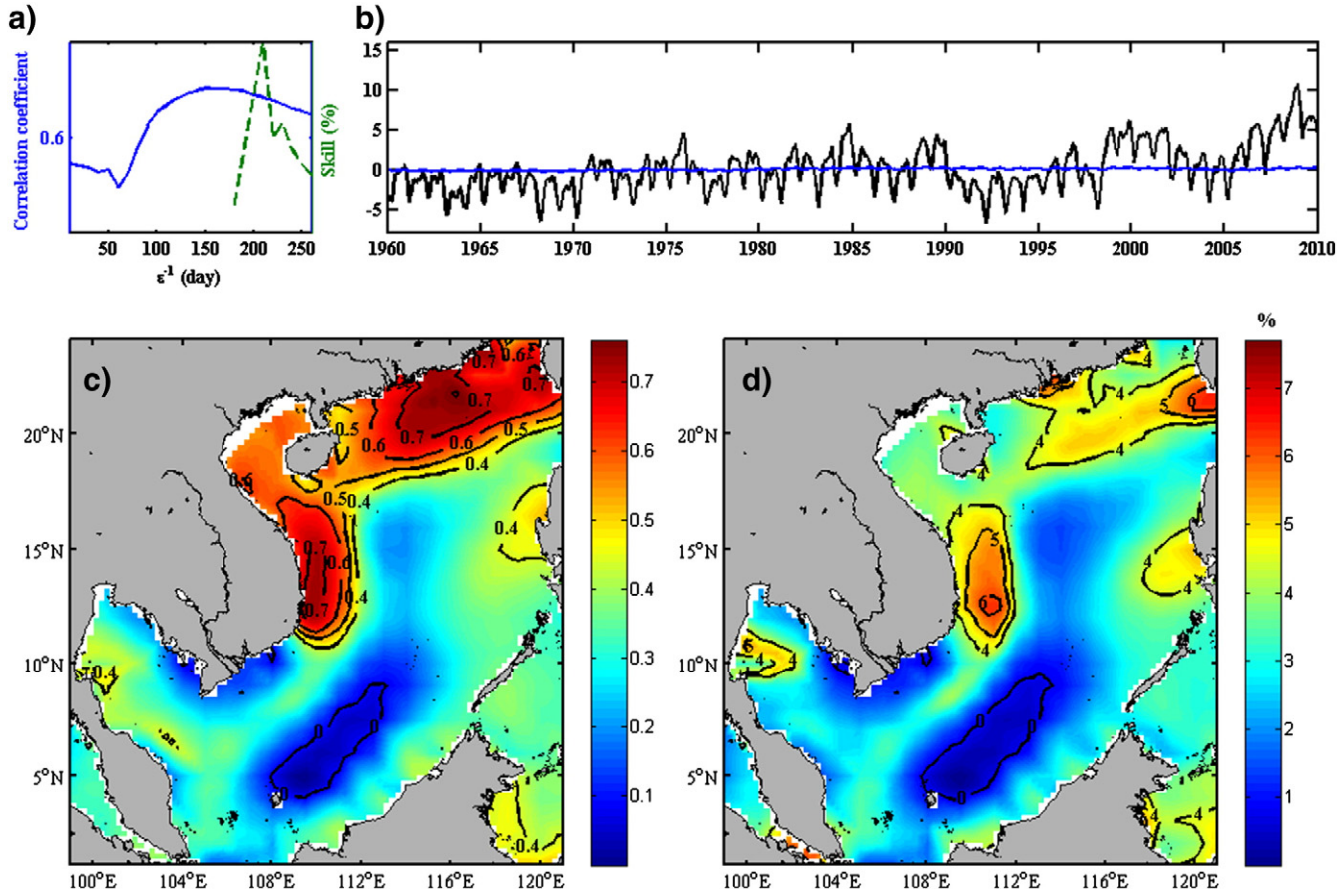


**Fig. 8.** (a) Correlation coefficient and skill of the $h_{water}$ as a function of the dissipation rate $\varepsilon$. (b) $h_{water}$ (blue line) vs. SSH(black line). (c) Correlations between $h_{water}$ and SSH. (d) Distribution of skill (%) of $h_{water}$ in accounting for the variance of SSH. Note, correlation coefficients exceeding 0.5 and skill exceeding 7% in the SCS are chosen in a). $\varepsilon_2{-}^1$ equals 200 $d$ in (b)–(d).

indicated that Luzon and Vietnam cold eddies are closely related to wind stress curl. Liu et al. (2001a,b) pointed out that the seasonal variation of SSH was due to wind seasonal variation in SCS. The upwelling of the west off Luzon in winter and offshore of central Vietnam in summer are almost related to wind stress curl (Qu, 2000; Xie S. P. et al., 2003; Yang and Liu, 2003). It is thus clear that the sea surface wind stress is an important forcing source for ocean from atmosphere.

In order to investigate the relationship between SSH and sea surface wind stress curl in the SCS, we draw the time series plot of them (Fig. 9). There is a good corresponding relation between them, and the maximum correlation coefficient is 0.44 when wind stress curl annomaly leads SSH by about 4 months.

Ekman pumping is the simplest dynamic mechanism of wind-induced SSH. Cyclonic (anticyclonic) wind stress curl produces sea surface divergence (convergence), and leads to SSH decreasing (increasing).

Several investigators in the past have suggested that the SSH may simply have the relevance of Ekman dynamics (Kelly et al., 1993; Bhaskaran et al., 1993; Lagerloef, 1995; Stammer, 1997; Vivier et al., 1999; Cummins and Lagerloef, 2002, 2004; Capotondi et al., 2005; Cabanes et al., 2006; Qiu and Chen, 2006). Ekman pumping model driven by the local wind stress forcing can also be written in the form of a first-order autoregressive process Markov model by the local Ekman pumping. Hasselmann (1977) applied stochastic climate models to examine the response to Ekman pumping at station P and over the northeast Pacific. Lagerloef (1995) applied a local stochastic

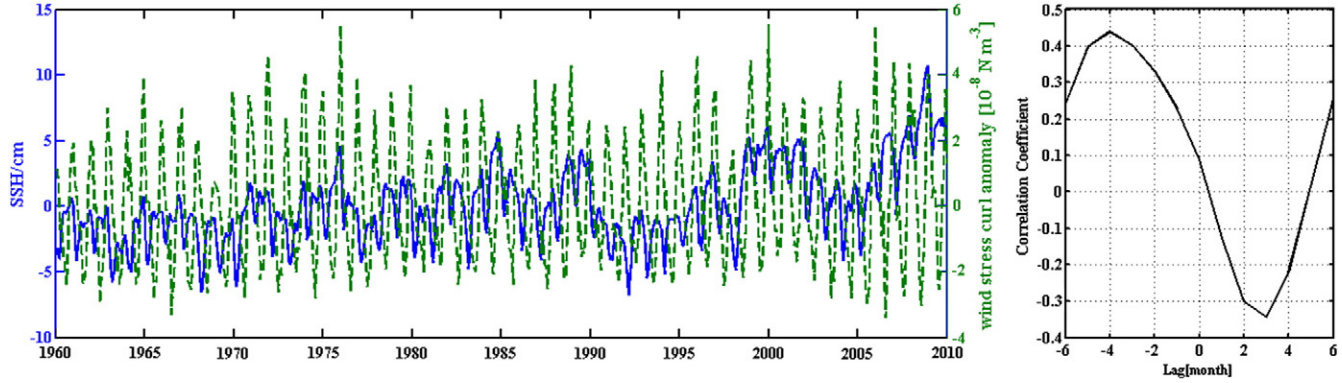


**Fig. 9.** Comparison between SSH and wind stress curl anomaly. Positive lags here indicate SSH leads the wind stress curlz anomaly.

climate model (Frankignoul and Hasselmann, 1977; Hasselmann, 1977) and showed through canonical correlation analysis that time-dependent Ekman pumping dynamics could account for low frequency dynamic height variability over the Gulf of Alaska. Cummins and Lagerloef (2002) demonstrated that a local Markov model driven by Ekman pumping to examine the structure of pycnocline depth variability forced by the dominant patterns of anomalous Ekman pumping over the northeast Pacific (30°–60°N, 180°–240°E) during 1948–2000. Cummins and Lagerloef (2004) further investigated the performance of the local Ekman pumping model of their old work in 2002, by estimating its ability to reproduce observed SSH variability in the northeast Pacific during 1993–2003, and concluded that interannual variability in the Gulf of Alaska is dominated by the local response to wind forcing. Qiu and Chen (2006) used the same model to examine the Ekman dynamics in which the SSH changes are determined by the local wind stress curl forcing.

For the present application, the Markov model is expressed as:

$$\frac{\partial h_{EK}}{\partial t} = -\frac{g' \,\mathrm{curl}\tau}{\rho_0 g f} - \varepsilon_3 h_{EK} \tag{10}$$

with the solution

$$h_{EK}(x,y,t) = -\frac{g'}{\rho_0 g f}\int_t \mathrm{curl}\tau(x,y,t)\exp\left[-\varepsilon_3\left(t-t'\right)\right]dt' \tag{11}$$

where $h_{EK}$ is the wind-induced SSH, $g'$ is the reduced gravity, $g$ is gravity constant, $\rho_0$ is the reference density, $f$ is the Coriolis parameter, curl$\tau$ is the vertical component of wind stress curl anomalies, and $\varepsilon_3$ is the Newtonian dissipation rate with the units of the inverse of time. To evaluate the Ekman pumping-induced $h_{EK}(x, y, t)$ field from Eq. (10), we adopt the following parameter values: $g' = 0.03$ m/s$^2$, $\rho_0 = 1024$ kg/m$-^3$. Eq. (10) is forced with monthly wind stress curl anomalies derived from ECMWF ORA-S3 for the period 1960–2009.

Fig. 10 shows calculated results of $h_{EK}$ based on the local Markov model. $\varepsilon_3^{-1}$ equals 60 $d$ in Fig. 10b–d. $h_{EK}$ presents a strong seasonal signal and its amplitude is 3.34 cm including annual amplitude of 2.98 cm (Fig. 10b). The east SCS is , for the most part, high correlation coefficients and skills region. Correlation coefficients mostly exceed 0.5 and $h_{EK}$ can account for above 30% of the SSH in this region.

It is worth noting that the total amplitude of $h_{heat}$ and $h_{EK}$ is larger than that of SSH. As previously stated, skill ranges between $-\infty$ and 1. High values for skill ($S \rightarrow 1$) indicate that observed and calculated SSH are both well correlated and of the same magnitude. Negative values denote low or negative correlations or larger magnitude for SSH. Buoyancy Forcing and Markov models can only explain part of SSH. For example, skill of $h_{EK}$ in the south SCS is below $-120\%$. Checking $h_{EK}$ in this area, we found $h_{EK}$ has high correlations but larger magnitude for SSH. Region-averaged $h_{EK}$ will inevitably produce errors. In addition, difference of SSH phase in some region can also cause this problem. There are other causes to affect SSH in the low skill region (the Kuroshio, rivers, steric height caused by temperature and salinity in the lower ocean, for example).

## 6. Steric component related to subsurface water in SSH

### 6.1. Interannual subsurface TSSL variability

Analysis of SSH induced by buoyancy flux and wind stress only revealed seasonal variations, but large timescale can't be explained

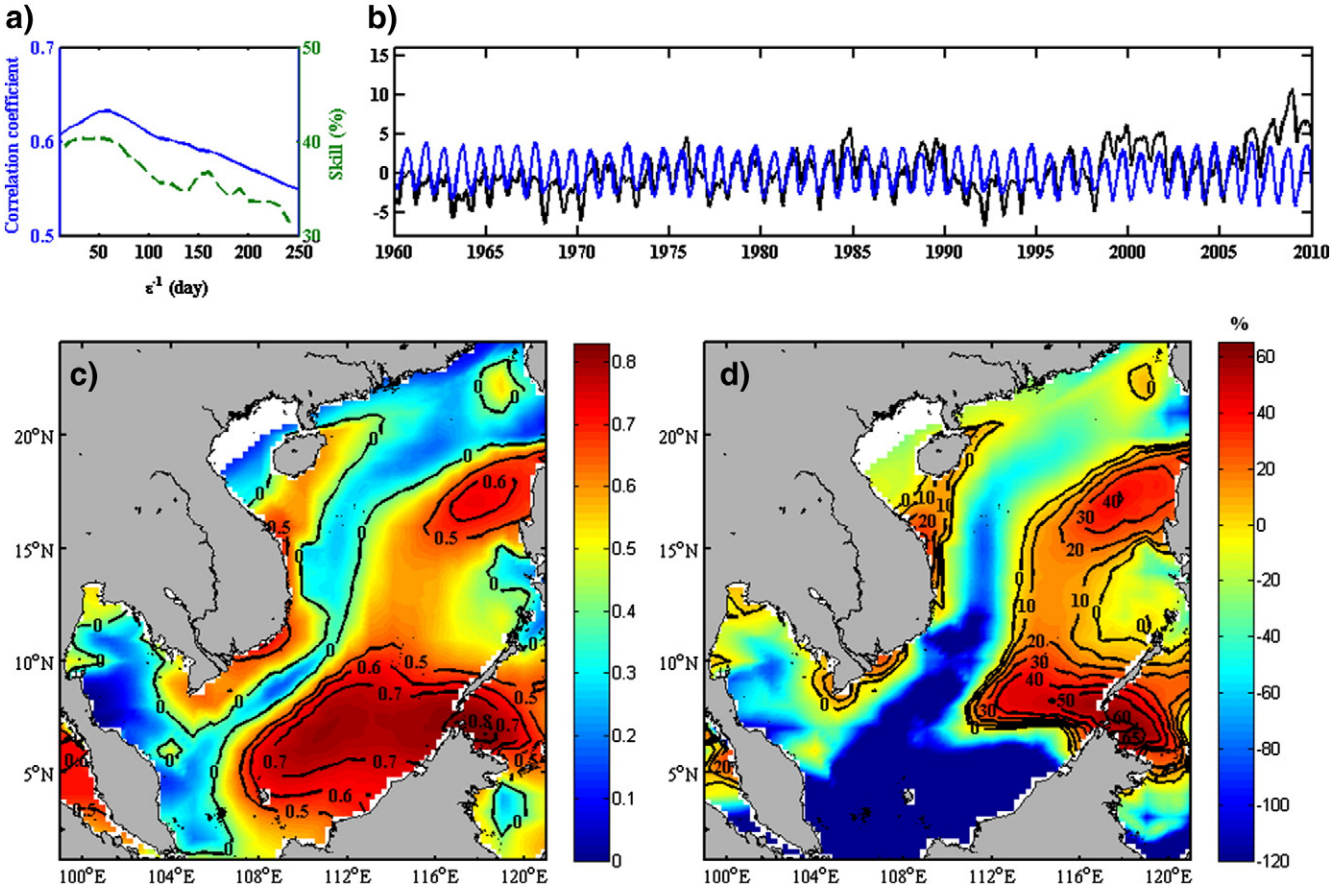


**Fig. 10.** (a) Correlation coefficient and skill of the $h_{EK}$ as a function of the dissipation rate $\varepsilon$. (b) $h_{EK}$ (blue line) vs. SSH (black line). (c) Correlations between $h_{EK}$ and SSH. (d) Distribution of skill (%) of $h_{EK}$ in accounting for the variance of SSH. Note, correlation coefficients exceeding 0.5 and skill exceeding 30% in the SCS are chosen in (a). In (b)–(d), $\varepsilon_3^{-1} = 60$ $d$.

(Figs. 7 and 10). To solve this, we calculate TSSL in the upper 1500 m SCS. We can get a close relation (correlation coefficient is 0.76) between TSSL and SSH (Fig. 11b). TSSL can account for 88.5% of the SSH in the SCS. TC can explain about 90% of TSSL, which is dominated compared with SC in the steric height changes.

TSSL in the upper 1500 m includes large timescale, but TSSL in the mixed layer only include seasonal signals. So we have to believe low frequency signals beneath the mixed layer in the SCS. As shown in Fig. 12, TSSL below the mixed layer has the same large-scale variation with the SSH residual (low-pass filtered over 13 months).

To better understand TSSL in different layers below MLD, we plot their time series in Fig. 13. There are distinct interannual variations in the SCS subsurface layer (100-300 m), especially in the depth of 100–200 m.

Fig. 14 shows comparisons between subsurface layer TSSL (sub-TSSL) and SOI/PDO/NPGO. Their correlations are 0.44, −0.27, and 0.48, respectively. The interannual variations of SSH are related to the SCS subsurface water and affected by ENSO/PDO/NPGO.

### 6.2. Possible mechanism between sub-TSSL and ENSO/PDO/NPGO

Based on the ocean dynamics and numerical model experiments, Qu et al. (2004) emphasized the role of oceanic bridge and pointed out that the water transport of Luzon Strait between the SCS and the Pacific Ocean is a key process conveying ENSO signal into the SCS and influencing its circulation and heat budget. The volume transports between the SCS and the adjacent oceans and the anomalous Ekman pumping contribute a lot for SSH (Rong et al., 2007). Interannual variability of SSH is closely related to water exchange in the SCS. Luzon Strait transport (LST) is an important process conveying the impact of ENSO to the SCS.

LST can be affected by westward Rossby waves in recent studies (Sheu et al., 2010; Zhang et al., 2010; Zheng et al., 2011). Rossby wave originate from the eastern/central North Pacific, which is the region where the wind stress curl has its largest amplitude and is the action center of the PDO-related wind anomalies (Mantua et al., 1997; Qiu 2003). Wind stress curl anomalies over the eastern/central North Pacific Ocean generate rossby wave through Ekman divergence (convergence). LST modulates interannual and decadal variability on the western boundary via changes in the wind stress curl field of the eastern/central North Pacific. Recently, it is found that in the middle latitudes, the SSH anomalies are largely determined by wind stress curl variations associated with the forcing of NPGO, rather than the PDO (Ceballos et al., 2009; Zhang et al., 2011). Rossby waves carry the signature of the NPGO across the eastern to the western boundary.

There are also striking responses of the Balabec Strait and Mindoro Strait transport to ENSO. More water flow out the SCS when an El Niño is in its developing stage and seem to balance the increased LST (Rong et al., 2007). Water exchange between SCS and Sulu sea through Balabec Strait and Mindoro Strait. Surface water is dominantly controlled by atmosphere forcing, and subsurface water is affected by climatic mode. Interestingly, spatial structure of SSH interannual variability is dominantly distributed over the Sulu Sea in Section 3.2. Shallower passages compared to Mindoro Strait connect the Sulu Sea to the Sulawesi Sea and through the Philippine archipelago to the west Pacific. Sulawesi Sea and west Pacific are equally important.

## 7. Summary and conclusion

In this paper, we investigate characteristics and the mechanisms of SSH in 50 years (1960–2009) of ECMWF ORA-S3 data in the SCS.

Using stochastic dynamic analytic method to separate periodic signal of SSH, we can find SSH in the SCS displays a distinct annual cycle with minimum in February and maximum in August, and its amplitude is 1.81 cm (Fig. 1). The semiannual amplitude is 0.99 cm. SSH also displays obviously interannual variability. The SSH in the SCS is coherent with the ENSO/PDO/NPGO on large timescale based on the lead-lag relationship. During El Nino (La Nina) year, SOI has a minimum (maximum) value, and SSH is low(high). It is evidenced that the SSH variations in the SCS are strongly modulated by ENSO: their changes are the same phase, negative phase of SOI (El Niño event) corresponding to negative SSH; SOI positive phase (La Nina) corresponding to positive SSH. When PDO(NPGO) is warm (cold) phase, SSH have low values, and vice versa.

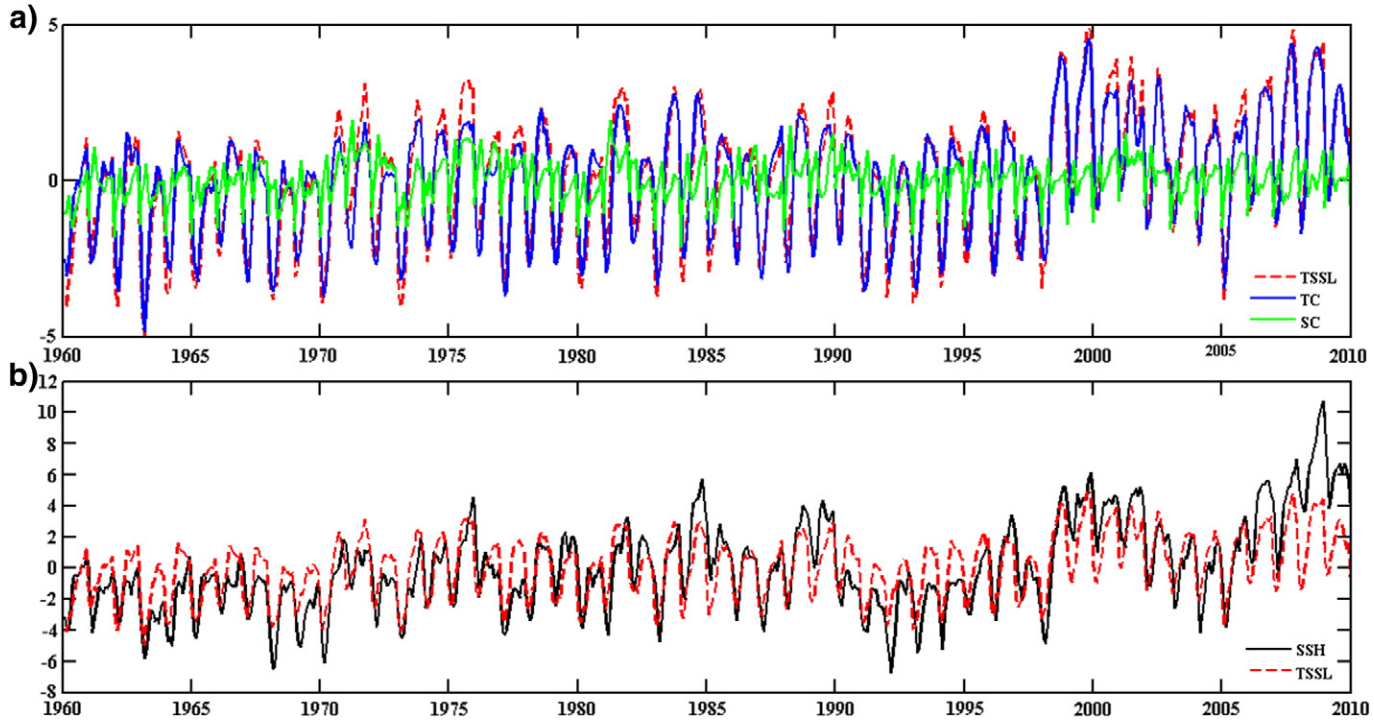


**Fig. 11.** (a) Time series of TSSL, TC and SC. (b) SSH (solid black line) vs. modeled TSSL (dashed red line). Units: cm.

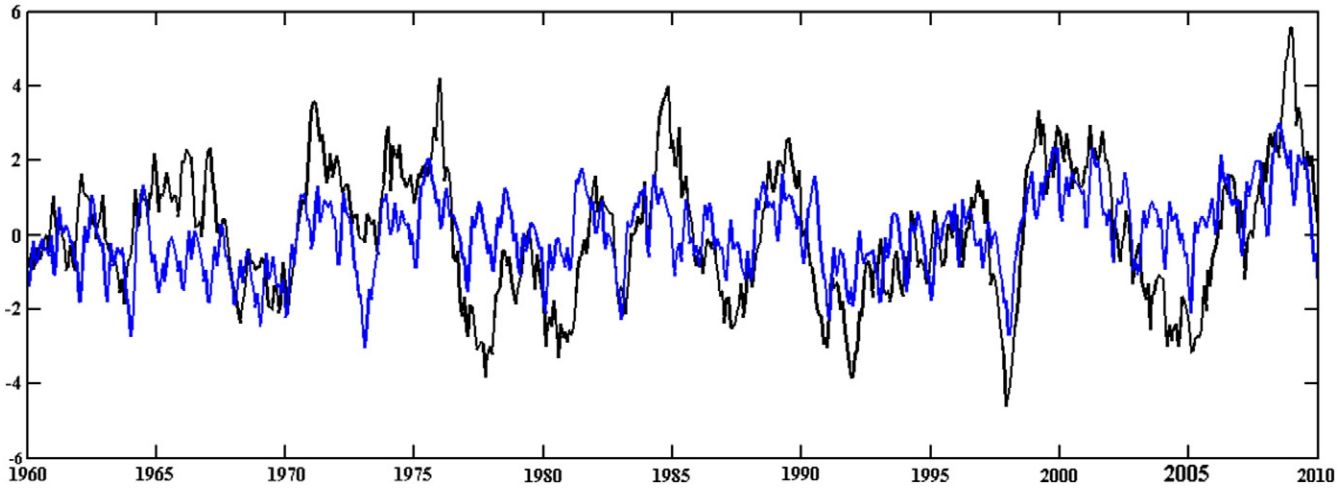


**Fig. 12.** The sum of TSSL below the ML in the upper 1500 m vs. SSH residual (like in Section 3).

Seasonal variations of SSH are induced by buoyancy fluxes and local wind stress. SSH induced by buoyancy fluxes is determined by changes of heat fluxes in the upper ocean. The effect of fres$h_{water}$ fluxes can be neglected. Correlation coefficients between $h_{heat}$ and SSH can reach above 0.5 in the northeast SCS. The seasonal amplitude of $h_{heat}$ in the SCS is 2.3 cm including annual amplitude of 1.67 cm. $h_{heat}$ displays significant seasonal variability (Fig. 10b). Fig. 10c and d shows distribution of correlations and skill between $h_{heat}$ and SSH. Heat fluxes have a great effect on SSH in the northeast SCS and its contribution to SSH is above 30% in this region (Fig. 10d).

The $h_{EK}$ based on the local Markov model has strong correlation relationship with the SSH in the east SCS (Fig. 10c). $h_{EK}$ presents a strong seasonal signal and its amplitude is 3.34 cm, with annual amplitude 2.98 cm. The $h_{EK}$ derived from Ekman pumping can account for 20–65% of the SSH in the east SCS (Fig. 10d). Hence, the local wind stress's contribution to seasonal SSH in the upper ocean is dominant, and the buoyancy's contribution is secondary. It is worth noting that the total amplitude of $h_{heat}$ and $h_{EK}$ is larger than that of SSH. This is mainly because Buoyancy Forcing and Markov models can only explain part of SSH in the upper ocean. There are other causes to affect SSH (the Kuroshio, rivers, steric height caused by temperature and salinity in the lower ocean, for example).

On interannual timescale, SSH are closely related to the SCS subsurface water (depth about 100–300 m). The correlation coefficients between TSSL in the subsurface layer and SOI/PDO/NPGO are 0.44, −0.27, and 0.48, respectively. The sub-TSSL presents low/high value at interannual variability when PDO and ENSO have strong positive/negative phase signal. The phase of NPGO agrees with that of sub-TSSL. When NPGO is warm (cold) phase, sub-TSSL have high (low) values, and vice versa. Namely, ENSO/PDO/NPGO affect the temperature

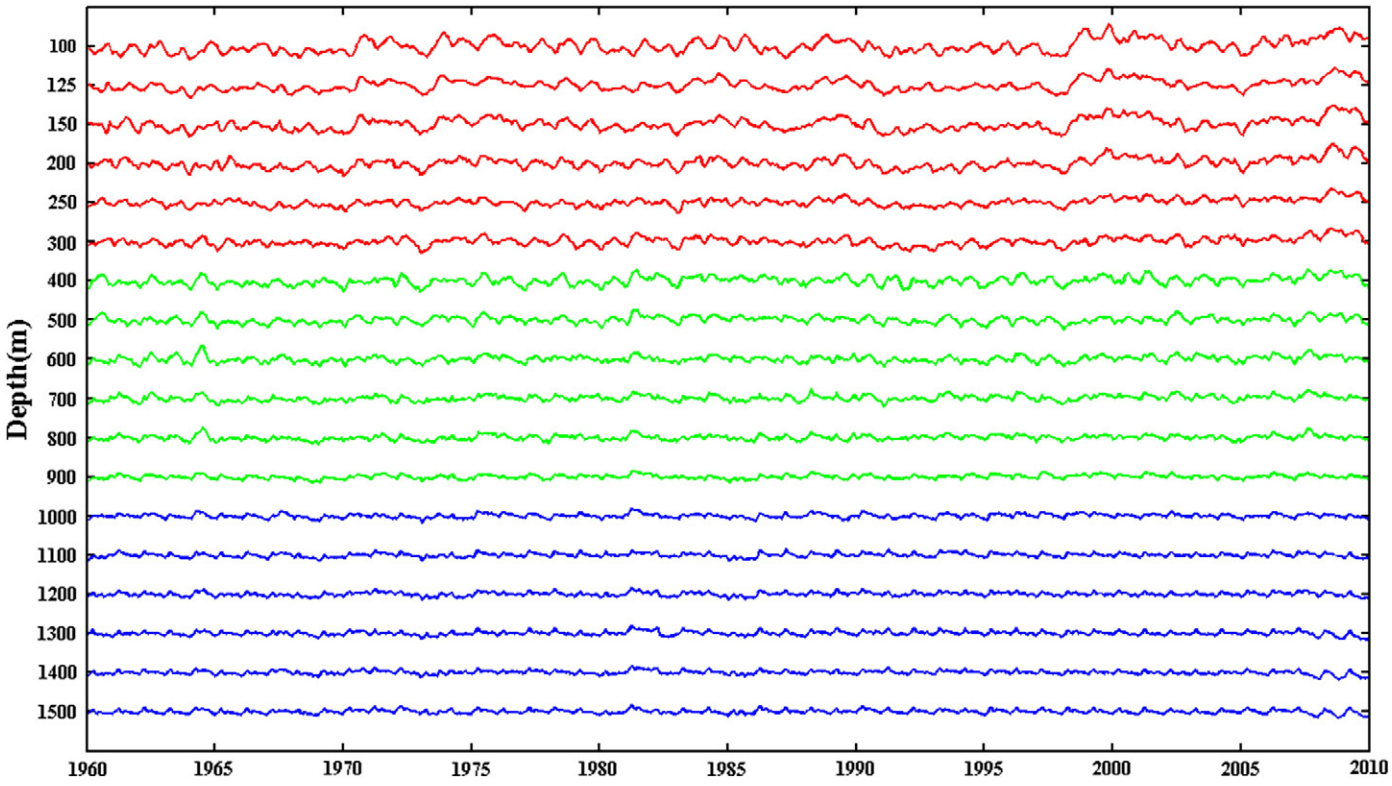


**Fig. 13.** TSSL below the ML in the upper 1500 m.

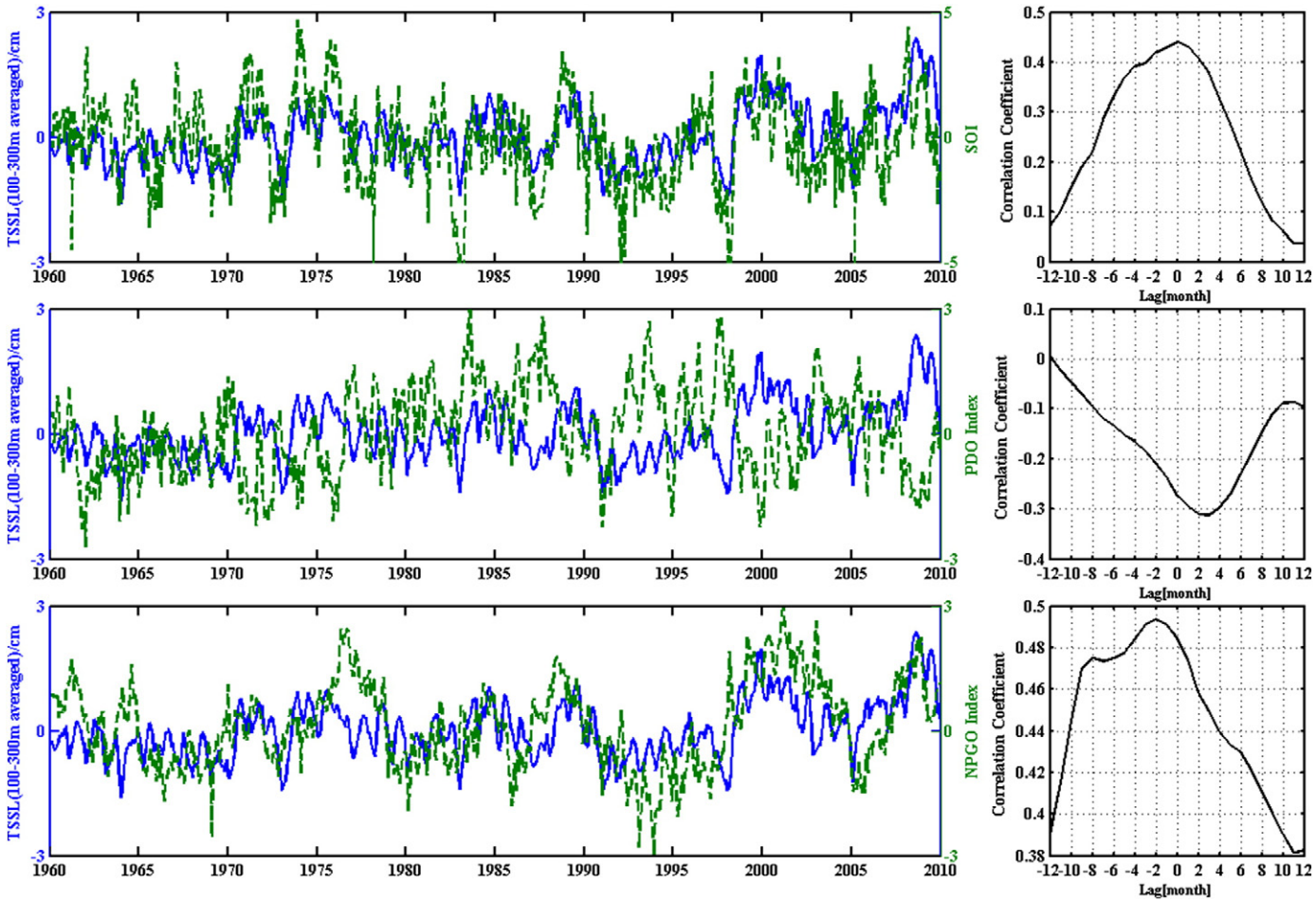


**Fig. 14.** Comparison between sub-TSSL (solid blue line) and climate indices (SOI/PDO/NPGO) (dashed green line). Right plates are their lagged correlation. Positive lags here indicate the lead of SOI/PDO/NPGO over the sub-TSSL.

and salinity changes of the subsurface water in the SCS, and further the interannual variability of SSH.

## Acknowledgements

This work was supported by the National Natural Science Foundation of China (Grant Nos. 41076005 and 41176009) and the National Basic Research Program of China (Grant No. 2012CB955602). Support was also provided by Public science and technology research funds projects of ocean (Grant No. 201005019).The authors benefited from discussions with Qinyu Liu. We thank to ECMWF and Ishii(6.9) for providing atmosphere and ocean data.

## References

Anderson, D., Balmaseda, M., 2005. Overview of ocean models at ECMWF, *Seminar on Recent Developments in Numerical Methods for Atmospheric and Ocean Modelling*. ECMWF Seminar Proceedings, ECMWF, pp. 103–111.

Balmaseda, M., 2004. Ocean data assimilation for seasonal forecasts, *Seminar on Recent Developments in Data Assimilation for Atmosphere and Ocean*. ECMWF Seminar Proceedings, ECMWF, pp. 301–326.

Balmaseda, M., Vidard, A., Anderson, D., 2008. The ECMWF Ocean Analysis System: ORA- S3. Monthly Weather Review 136, 3018–3034.

Bhaskaran, S., Lagerloef, G., Born, G., Emery, W., Leben, R., 1993. Variability in the gulf of Alaska from geosat altimetry data. Journal of Geophysical Research 98 (C9), 16, 311–16, 330.

Boyer, T.P., Antonov, J.I., Garcia, H.E., Johnson, D.R., Locarnini, R.A., Mishonov, A.V., Pitcher, M.T., Baranova, O.K., Smolyar, I.V., 2006. World Ocean Database 2005. In: Levitus, S. (Ed.), NOAA Atlas NESDIS 60. U.S. Government Printing Office, Washington, D.C., 190 pp. (DVDs).

Cabanes, C., Huck, T., Colin de Verdière, A., 2006. Contributions of wind forcing and surface heating to interannual sea level variations in the Atlantic ocean. Journal of Physical Oceanography 36 (9), 1739–1750.

Capotondi, A., Alexander, M.A., Deser, C., Miller, A.J., 2005. Low-frequency pycnocline variability in the northeast Pacific. Journal of Physical Oceanography 35 (8), 1403–1420. doi:10.1175/JPO2757.1.

Carton, J.A., Giese, B.S., Grodsky, S.A., 2005. Sea level rise and the warming of the oceans in the SODA ocean reanalysis. Journal of Geophysical Research 10. doi:10.1029/2004JC002817.

Cazenave, A., Dominh, K., Gennero, M.C., Ferret, B., 1998. Global mean sea level change observed by TOPEX/POSEIDON and ERS-1. Physics and Chemistry of the Earth 23, 1069–1075. doi:10.1016/S0079-1946(98)00146-3.

Cazenave, A., Nerem, R.S., 2004. Present-day sea level change: observations and causes. Geophysical Research Letters 42, RG3001.

Ceballos, L., Di Lorenzo, E., Schneider, N., Taguchi, B., 2009. North Pacific Gyre Oscillation synchronizes climate fluctuations in the eastern and western North Pacific. Journal of Climate. doi:10.1175/2009JCLI2848.1.

Chen, J.L., Shum, C.K., Wilson, C.R., Chambers, D.P., Tapley, B.D., 2000. Seasonal sea level change from Topex/Poseidon observation and thermal contribution. Journal of Geodesy 73 (12), 638–647. doi:10.1007/s001900050002.

Cummins, P., Lagerloef, G., 2002. Low-frequency pycnocline depth variability at ocean weather station in the northeast Pacific. Journal of Physical Oceanography 32, 3207–3215.

Cummins, P., Lagerloef, G., 2004. Wind-driven interannual variability over the northeast Pacific Ocean. Deep Sea Research I 51, 2105–2121.

Deser, C., Alexander, M.A., Timlin, M.S., 1999. Evidence for a wind-driven intensification of the Kuroshio Current Extension from the 1970s to the1980s. Journal of Climate 12, 1697–1706.

Frankignoul, C., Hasselmann, K., 1977. Stochastic climate models, Part II: application to sea-surface temperature anomalies and thermocline variability. Tellus 29, 289–305.

Frankignoul, C., Müller, P., Zorita, E., 1997. A simple model for the decadal response of the ocean to stochastic wind forcing. Journal of Physical Oceanography 27, 1533–1546.

Hasselmann, K., 1977. Stochastic climate models, part I: theory. Tellus 28, 473–484.

Ishii, M., Kimoto, M., 2009. Reevaluation of historical ocean heat content variations with time-varying XBT and MBT depth bias corrections. Journal of Oceanography 65, 287–299.

Ishii, M., Kimoto, M., Kachi, M., 2003. Historical ocean subsurface temperature analysis with error estimates. Monthly Weather Review 131, 51–73.
Ishii, M., Shouji, A., Sugimoto, S., Matsumoto, T., 2005. Objective analyses of SST and marine meteorological variables for the 20th century using COADS and the Kobe Collection. International Journal of Climatology 25, 865–879.
Ishii, M., Kimoto, M., Sakamoto, K., Iwasaki, S.I., 2006. Steric sea level changes estimated from historical ocean subsurface temperature and salinity analyses. Journal of Oceanography 62 (2), 155–170.
Kara, A.B., Rochford, P.A., Hurlburt, H.E., 2000. An Optimal Definition for Ocean Mixed Layer Depth. Journal of Geophysical Research 105 (C7), 16803–16821.
Kelly, K.A., Caruso, M.J., Austin, J.A., 1993. Wind-forced variations in sea surface height in the Northeast Pacific Ocean. Journal of Physical Oceanography 23, 2392–2411.
Lagerloef, G.S.E., 1995. Interdecadal variations in the Alaska gyre. Journal of Physical Oceanography 25 (10), 2242–2258.
Liu, Q.Y., Yang, H.J., Jia, Y.L., Gan, Z.J., 2001a. The numerical simulation of the seasonal variation of the sea surface height in the South China Sea. Acta Oceanologica Sinica 23 (2), 9–17.
Liu, Z.Y., Yang, H.J., Liu, Q.Y., 2001b. Regional dynamics of seasonal variability in the South China Sea. Journal of Physical Oceanography 31.
Lombard, A., Cazenave, A., Le Traon, P.Y., Ishii, M., 2005a. Contribution of thermal expansion to present-day sea-level change revisited. Global and Planetary Change 47, 1–16.
Lombard, A., Cazenave, A., DoMinh, K., Cabbanes, C., Nerem, R.S., 2005b. Thermosteric sea level rise for the past 50 year; comparison with tide gauges and inference on water mass Contribute. Global and Planetary Change 48, 303–312.
Mantua, N.J., Hare, S.R., Zhang, Y., Wallace, J.M., Francis, R.C., 1997. A Pacific decadal climate oscillation with impacts on salmon. Bulletin of the American Meteorological Society 78, 1069–1079.
Miller, A.J., Cayan, D.R., White, W.B., 1998. A westward intensified decadal change in the North Pacific thermocline and gyre-scale circulation. Journal of Climate 11 (12), 3112–3127.
Nerem, R.S., Haines, B.J., Hendricks, J., Minster, J.F., Mitchum, G.T., White, W.B., 1997. Improved determination of global mean sea level variations using TOPEX/Poseidon altimeter data. Geophysical Research Letters 24 (11), 1331–1334.
Patttullo, J., Munk, W., Revelle, R., Strong, E., 1955. The seasonal oscillation in sea level. Journal of Marine Research 14, 88–155.
Qiu, B., 2002. Large-scale variability in the midlatitude subtropical and subpolar North Pacific Ocean: observations and causes. Journal of Physical Oceanography 32 (1), 353–375.
Qiu, B., 2003. Kuroshio Extension variability and forcing of the Pacific decadal oscillations: responses and potential feedback. Journal of Physical Oceanography 33, 2465–2482.
Qiu, B., Chen, S.M., 2006. Decadal variability in the large-scale sea surface height field of the South Pacific Ocean: observations and causes. Journal of Physical Oceanography 36, 1751–1762.
Qu, T.D., 2000. Upper-layer circulation in the South China Sea. Journal of Physical Oceanography 30, 1450–1460.
Qu, T., Kim, Y.Y., Yaremchuk, M., Tozuka, T., Ishida, A., Yamagata, T., 2004. Can Luzon strait transport play a role in conveying the impact of ENSO to the South China Sea? Journal of Climate 17, 3644–3657.
Rong, Z.R., Liu, Y.G., Zong, H.B., Cheng, Y.C., 2007. Interannual sea level variability in the South China Sea and its response to ENSO. Global and Planetary Change 55 (4), 257–272.
Sasaki, Y.N., Shoshiro, M., Niklas, S., Takashi, K., Masami, N., Hideharu, S., 2008. Decadal sea level variability in the South Pacific in a global eddy-resolving ocean model hindcast. Journal of Physical Oceanography 38 (8), 1731–1746.
Schneider, N., Miller, A.J., Pierce, D.W., 2002. Anatomy of North Pacific decadal variability. Journal of Climate 15 (6), 586–605.
Seager, R., Kushnir, Y., Naik, N.H., Cane, M.A., Miller, J., 2001. Wind-driven shifts in the latitude of the Kuroshio-Oyashio Extension and generation of SST anomalies on decadal timescales. Journal of Climate 14 (22), 4249–4265. doi:10.1175/1520-0442.
Sheu, W.J., Wu, C.R., Oey, L.Y., 2010. Blocking and westward passage of eddies in the Luzon Strait. Deep Sea Res II 57 (19–20), 1783–1791. doi:10.1016/j.dsr2.2010.04.004.
Stammer, D., 1997. Steric and wind-induced changes in TOPEX/Poseidon large-scale sea surface topography observations. Journal of Geophysical Research 102 (C9), 20987–21009.
Sturges, W., Hong, B.G., 1995. Wind forcing of the Atlantic thermocline along 32°N at low frequencies. Journal of Physical Oceanography 25, 1706–1715.
Tabata, S., Thomas, B., Ramsden, D., 1986. Annual and interannual variability of steric sea level along line P in the Northeast Pacific Ocean. Journal of Geophysical Research 16, 1378–1398.
Taguchi, B., Xie, S.P., Schneider, N., Nonaka, M., Sasaki, H., Sasai, Y., 2007. Decadal variability of the Kuroshio Extension: observations and an eddy-resolving model hindcast. Journal of Climate 20 (11), 2357–2377.
UNESCO, 1987. International oceanographic Tables. UNESCO Technical Papers in Marine Science 4, 40.
Vidard, A., Balmaseda, M., Anderson, D., 2009. Assimilation of Altimeter Data in the ECMWF Ocean Analysis System 3. Monthly Weather Review 137, 1393–1408. doi:10.1175/2008MWR2668.1.
Vivier, F., Kelly, K.A., Thompson, L., 1999. Contributions of wind forcing, waves, and surface heating to sea surface observations in the Pacific Ocean. Journal of Geophysical Research 104 (C9), 20767–20788.
Wyrtki, K., 1961. Scientific results of marine investigation of the South China Sea and Gulf of Thailand. NAGA Report, 2, p. 195.
Xie, S.P., Xie, Q., Wang, D.X., Liu, W.T., 2003. Summer upwelling in the South China Sea and its role in regional climate variations. Journal of Geophysical Research 108 (C8), 3261. doi:10.1029/2003JC001876.
Yang, H.J., Liu, Q.Y., 2003. Foreed Rossby wave in the northern South China Sea. Deep Sea Research Part I 50, 917–926.
Zhang, Y.C., Zhang, L.F., Lü, Q.P., 2011. Dynamic mechanism of interannual sea surface height variability in the north Pacific subtropical gyre. Advances in Atmospheric Sciences 28 (1), 158–168.
Zhang, Z.G., Zhao, W., Liu, Q.Y., 2010. Sub-seasonal variability of Luzon Strait Transport in a high resolution global model. Acta Oceanologica Sinica 29 (3), 9–17. doi:10.1007/s13131-010-0032-0.
Zheng, Q.N., Tai, C.K., Hu, J.Y., Lin, H.Y., Zhang, R.H., Su, F.C., Yang, X.F., 2011. Satellite altimeter observations of nonlinear Rossby eddy–Kuroshio interaction at the Luzon Strait. Journal of Oceanography. doi:10.1007/s10872-011-0035-2.
Zuo, J.C., Chen, Z.Y., Zhou, T.H., 1996. A joint model of eigenanalysis and stochastic dynamics for analysing sea level variation along China coast. Acta Oceanologica Sinica 18 (2), 7–14.